Electronic Supplementary Information

The permeability of pillar arrays in microfluidic devices: an application of Brinkman's theory towards wall friction

Thejas Hulikal Chakrapani,[1] Hanieh Bazyar,[2] Rob G. H. Lammertink,[2] Stefan Luding[1]
and Wouter K. den Otter[1]

December 5, 2022

Contents

---

[1] Multi Scale Mechanics, MESA+ institute for nanotechnology and Faculty of Engineering Technology, University of Twente, P. O. Box 217, 7500 AE Enschede, The Netherlands.

[2] Soft Matter, Fluidics and Interfaces, MESA+ institute for nanotechnology and Faculty of Science and technology, University of Twente, P. O. Box 217, 7500 AE Enschede, The Netherlands.

List of Tables

List of Figures

S1 Experiments

S1.1 Fabrication of the microfluidic chip

The microfluidic chips are fabricated using standard photolithography and Deep Reactive Ion Etching (DRIE) techniques at the MESA+ Nanolab/clean room at the University of Twente. The process can be divided into three steps, namely etching of the pore network into the silicon (Si) wafer, etching the access holes through the Si wafer and finally bonding the finished Si wafer to a Mempax (Schott) wafer. The photolithography is done twice using two masks to make the pore network (leaving the pillars standing) and the access holes respectively. Before starting the photolithography, the Si wafers are thermally oxidized to get an SiO_2 layer of 1.7 μm, *i.e.* a hard mask. This is done by wet oxidation of an Si wafer at a temperature of 1150°C for 6 hours. After coating the Si wafer with a photoresist layer, the first mask is aligned with the wafer and the pillar pattern is transferred to the layer by exposure to UV light and resist development. The next step is to etch the protection SiO_2 layer and then the pillar pattern into the Si wafer (to a depth of 20 μm) using the DRIE technique (the Bosch process recipe is used). Then the photoresist layer is stripped using an oxygen plasma. A dicing foil is applied to the top of the wafer to protect it during powder-blasting. On the back a powderblast foil is applied (Harke I-HE dry-resist) and the access holes are defined via photolithography using the second mask. The access holes are etched using powder blasting. After powder blasting the foils are removed and the wafer is ultrasonically cleaned to remove any residual powder. Next the wafer is cleaned using piranha (H_2SO_4:H_2O_2, 3:1 vol.%) to remove any residual foil and rinsed with H_2O. The remaining SiO_2 layer is removed by dipping the wafer in buffered HF solution (BHF, 1:7) for 25 minutes and dried. The finished Si wafer is anodically bonded to the Mempax (Schott) wafer and diced into individual chips.

S1.2 Inspection of the pillar arrays

Zoomed-in images enabling inspection of individual pillars are provided in Figs S1 and S2. The side views illustrate the corrugated and slightly tapered structure of the pillars, while they appear nicely circular in the top view. Small residual ridges remain when the distances between the pillars are small relative to their diameters. The inlet/outlet of the microfluidic chips are shown in Fig. S3.

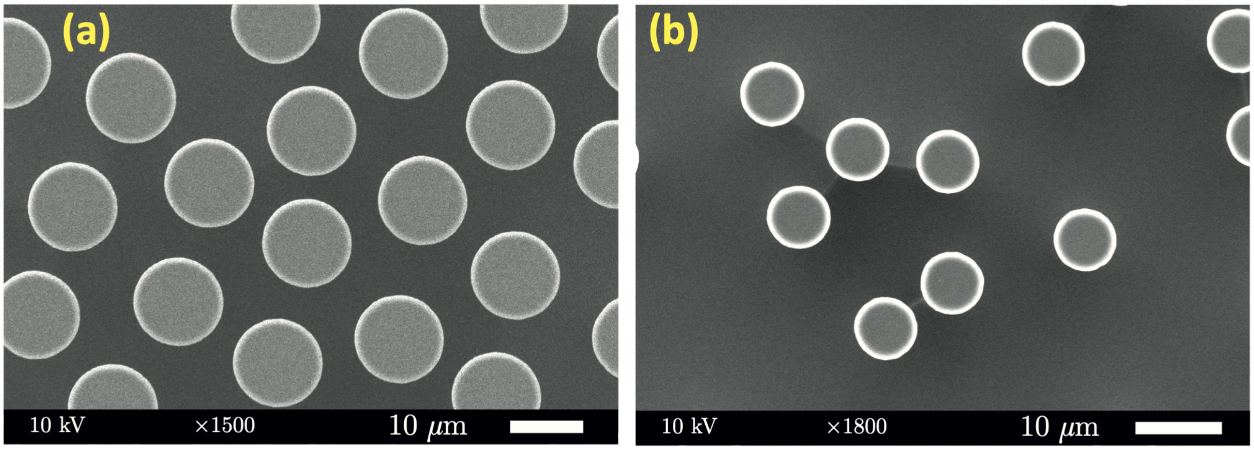

Figure S1: Zoomed-in SEM images showing top-views of the pillars at porosities of (a) 0.65 and (b) 0.87.

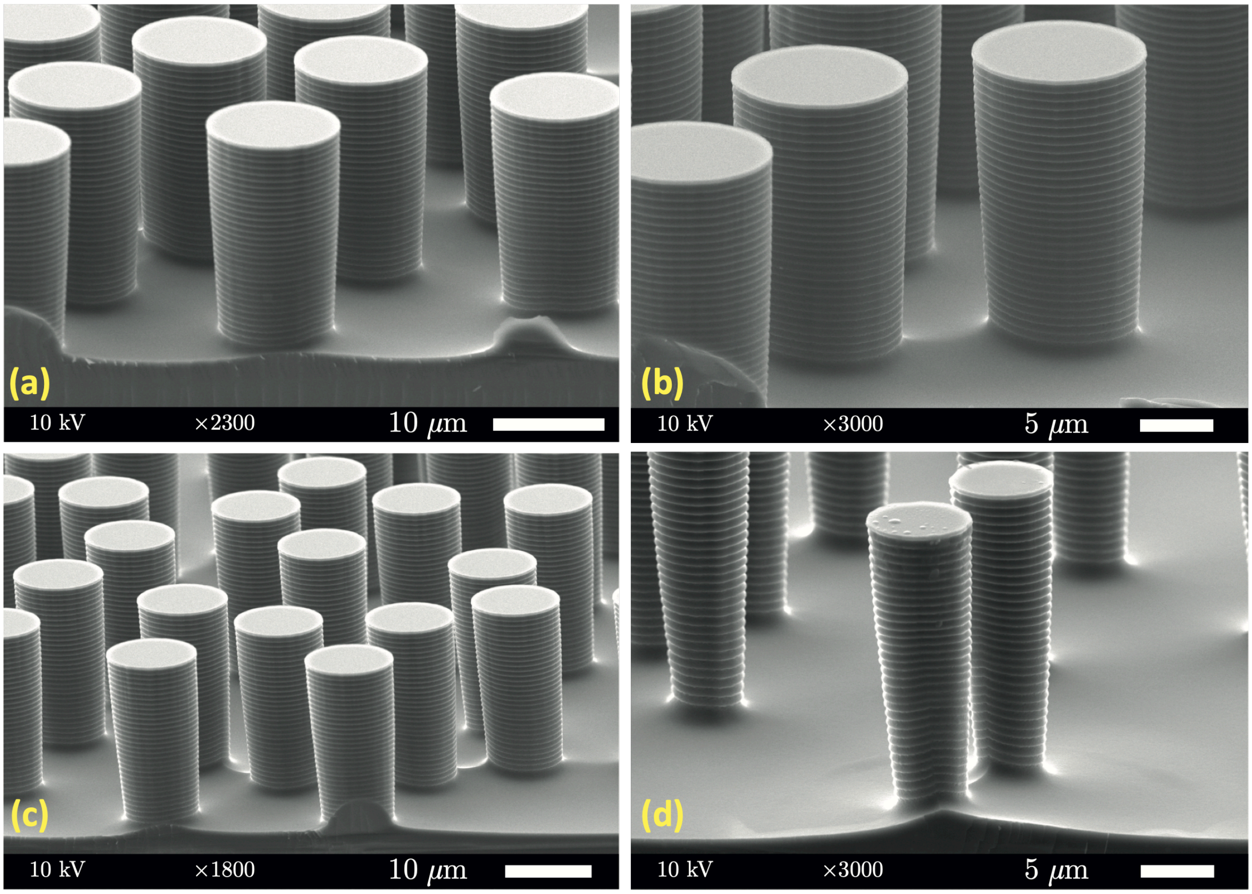

Figure S2: Zoomed-in SEM images showing side-views of the pillars at porosities of (a) 0.55, (b) 0.6, (c) 0.7 and (d) 0.85.

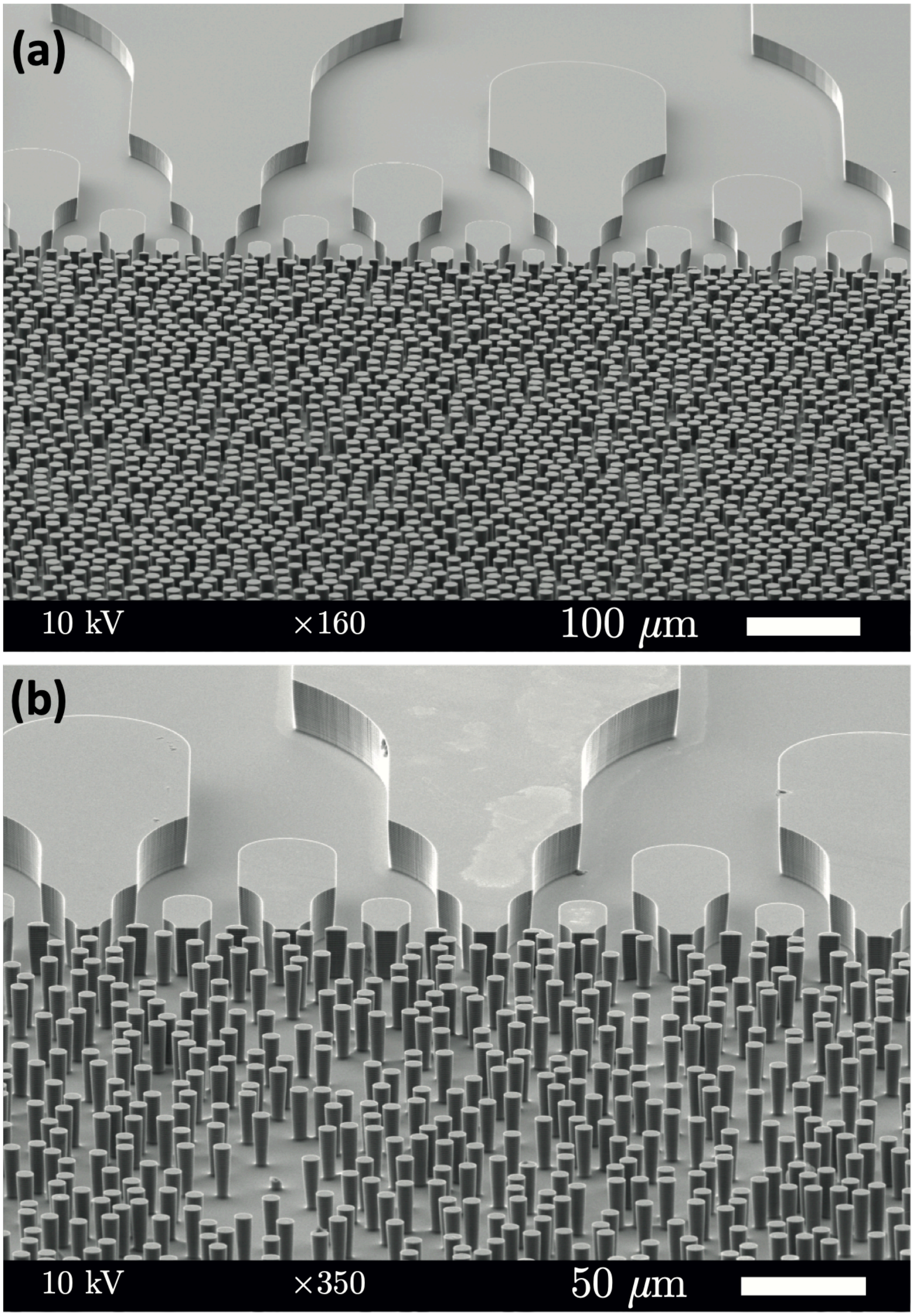

Figure S3: Side-view SEM images showing the inlet/outlet of the microfluidic chips with porosities of (a) 0.55 and (b) 0.85.

S1.3 Permeability measurements

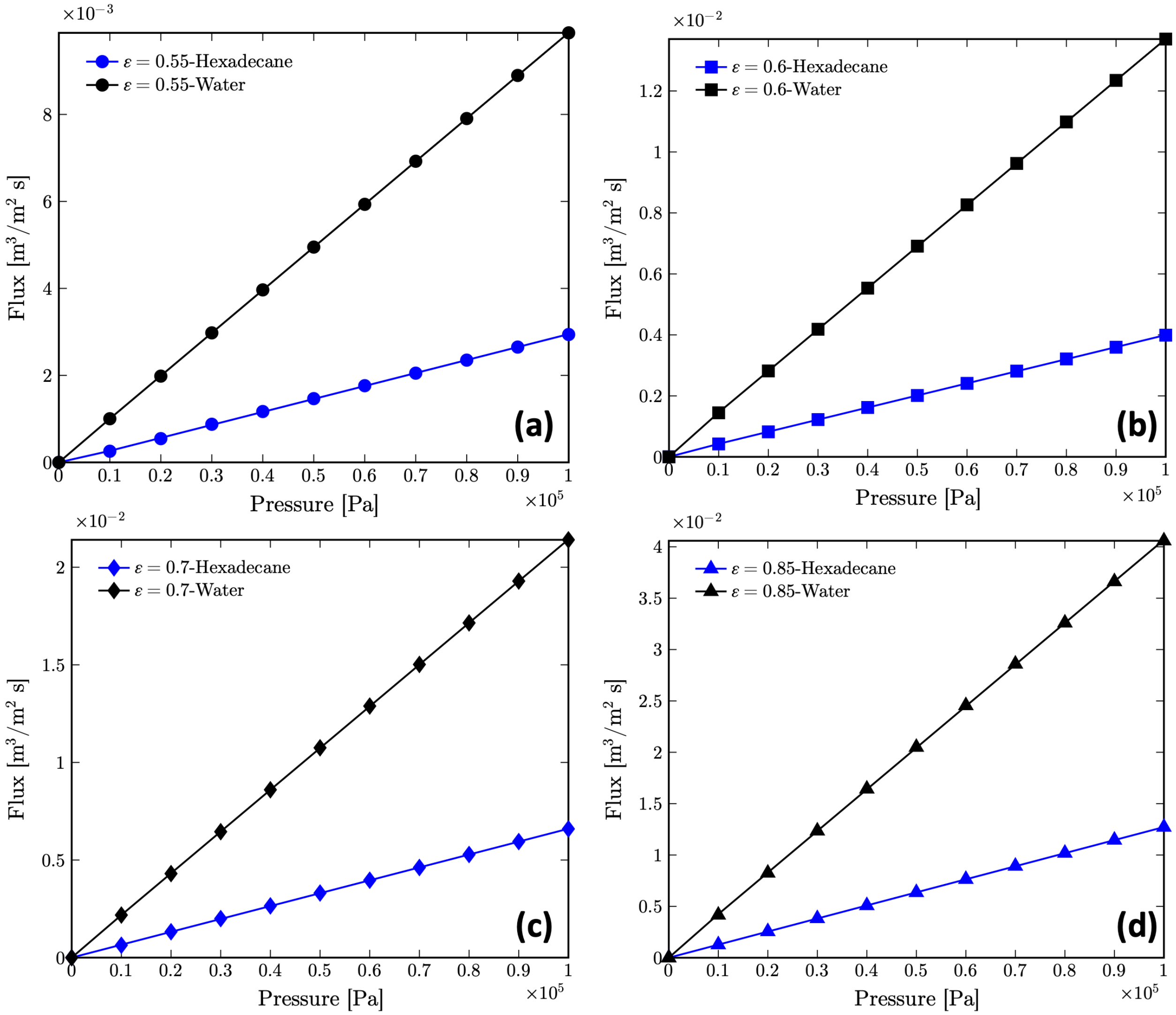

Figure S4: Water and hexadecane fluxes plotted against driving pressure for porosities of (a) 0.58, (b) 0.65, (c) 0.73 and (d) 0.87. The lines are linear fits whose slopes, by Darcy's law, yield the effective permeabilities collected in Table 1.

S2 MDPD simulations

S2.1 Simulations in 2D

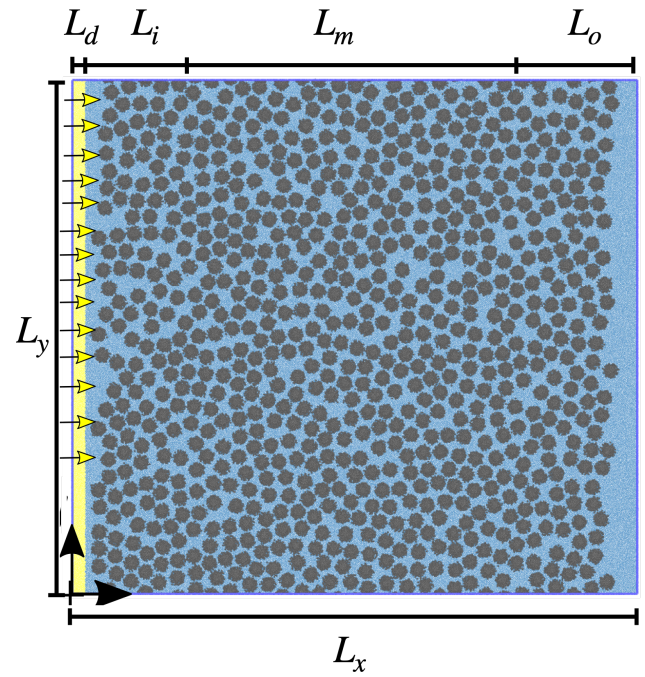

Figure S5: Top view of the simulation set-up for fluid (light blue) flowing through a disordered array of pillars (grey) in MDPD simulations, at a porosity of 55%. Periodic boundary conditions apply in the x and y directions. The length and width of the pillared region match the box dimensions of the Monte Carlo simulation that generated the pillar configuration. All fluid particles in the driving region of length L_d (yellow) experience a body force f_b in the x direction (yellow arrows). Consequently, the fluid outside this region experiences a pressure-driven flow. The measurement region of length L_m is separated from the driving region by the in-flow and out-flow regions of lengths L_i and L_o, respectively.

S2.1.1 Common parameters

Lengths that are common to all simulations, in 2D and 3D, are tabulated in Table S1; their definitions are illustrated in Figs S5 and S10. The diameters of the pillars are fixed at $d = 5\sigma$ in all simulations.

Table S1: Lengths of regions common to 2D and 3D simulations.

length	start	end	definition
L_d	0.0σ	5.0σ	length of driving region
L_i	5.0σ	$0.2L_x$	length of in-flow region
L_m	$0.2L_x$	$0.8L_x$	length of measurement region
L_o	$0.8L_x$	$1.0L_x$	length of out-flow region

In the next sections we tabulate the parameters and normalized permeabilities of all 2D systems simulated in this study. The various parameters listed in the ensuing tables are described in Table S2.

Table S2: Parameter definitions for 2D simulations.

parameters	definition
ε	porosity
N_{pil}	number of pillars
L_x	box length in x direction
L_y	box length in y direction
$L_{\|\|}$	length of pillared region
N_{part}	total number of particles
κ_p/d^2	normalized permeability

S2.1.2 Square lattices in 2D

The parameters for 2D simulations of flow through pillars arranged on square lattices and square lattices rotated over 45° are tabulated in Tables S3 and S4. The calculated permeabilities in the last column of both tables denote averages over simulations with body forces of $f_b = 0.1$, 0.2 and 0.3 ϵ/σ. All permeability values reported here and henceforth, are accurate to within 10% of the mean values.

Table S3: Simulation parameters of square lattices in 2D.

ε	N_{pil}	L_x [σ]	L_y [σ]	$L_{\|\|}$ [σ]	N_{part}	κ_p/d^2
0.50	100	146	31.33	125.33	27,497	0.004
0.55	100	153	33.03	132.11	30,357	0.006
0.60	100	161	35.03	140.12	33,896	0.01
0.65	100	170	37.45	149.80	38,260	0.02
0.70	100	182	40.45	161.80	44,258	0.03
0.75	100	198	44.31	177.25	52,739	0.05
0.80	100	219	49.54	198.17	65,212	0.09
0.85	75	192	57.21	171.62	66,012	0.2
0.90	75	231	70.06	210.19	96,814	0.3
0.95	50	219	99.08	198.17	130,389	1.0

Table S4: Simulation parameters of rotated square lattices in 2D.

ε	N_{pil}	L_x [σ]	L_y [σ]	$L_{\|\|}$ [σ]	N_{part}	κ_p/d^2
0.50	100	105	44.31	88.62	27,916	0.004
0.55	100	109	46.71	93.42	30,547	0.007
0.60	100	115	49.54	99.08	34,184	0.01
0.65	100	121	52.96	105.92	38,451	0.02
0.70	100	129	57.21	114.41	44,277	0.03
0.75	100	140	62.67	125.33	52,639	0.05
0.80	100	154	70.06	140.12	64,738	0.08
0.85	100	174	80.90	161.80	84,461	0.2
0.90	100	209	99.08	198.17	124,250	0.3
0.95	64	230	112.10	224.20	155,370	1.0

The permeabilities listed in Tables S3 and S4 are compared against several theories in Fig. 7 and against a more extensive set of theories in Fig. S6. These theories are detailed in Section S3.1. Note that the rotation of a square lattice of cylindrical pillars over 45° does not affect its permeability.[1,2]

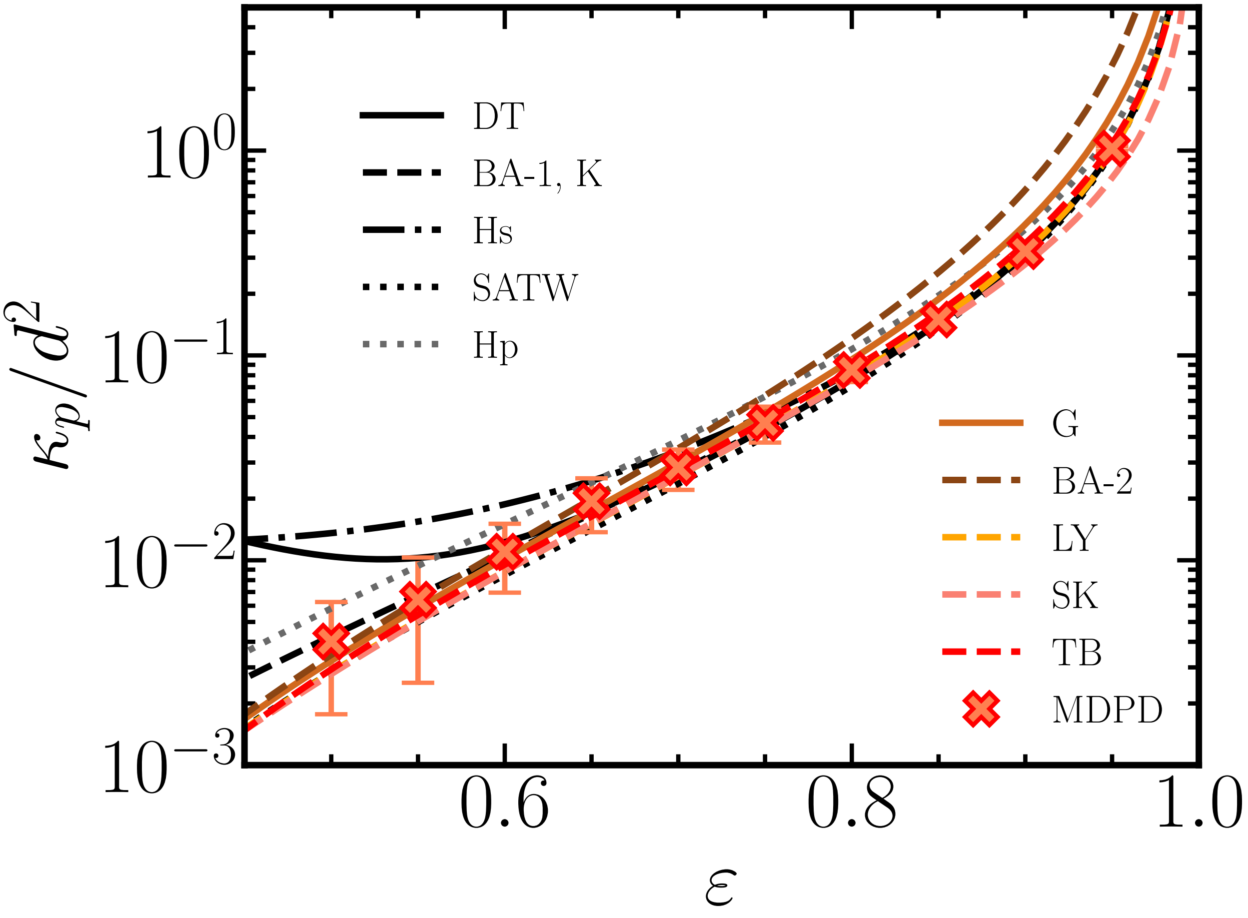

Figure S6: Permeabilities for transverse flow through square arrays of circular pillars, plotted against porosity. The markers show results from 2D MDPD simulations. The lines represent theoretical expressions by various authors, as indicated in the legend: Drummond and Tahir[1] (DT), Brushke and Advani[3] (BA, with BA-1 denoting lubrication theory and BA-2 the cell-configuration method), Kuwabara[4] (K), Hasimoto[5] (Hs), two expressions by Sangani and Acrivos[6] merged into one by Tsay and Weinbaum[7] (SATW), Happel[8] (Hp), Gebart[9] (G), Lee and Yang[10] (LY), Sahraoui and Kaviany[11] (SK) and Tamayol and Bahrami[12] (TB). All these expressions for the permeability can be found in Table S13. The lines in black and grey represent theories of the form $\kappa_p/d^2 = (32\phi)^{-1}\left[-\ln\phi + f(\phi)\right]$, where $\phi = 1 - \varepsilon$ is the solid volume fraction and f typically is a polynomial starting with the constant $-3/2$.

S2.1.3 Hexagonal lattices in 2D

The parameters for 2D simulations of flow through cylindrical pillars arranged on hexagonal lattices are tabulated in Tables S5. The permeabilities are plotted in Fig. S7, along with theoretical predictions detailed in Section S3.1.

Table S5: Simulation parameters of hexagonal lattices in 2D.

ε	N_{pil}	L_x $[\sigma]$	L_y $[\sigma]$	$L_{\|\|}$ $[\sigma]$	N_{part}	κ_p/d^2
0.50	120	98	58.32	80.81	34,355	0.006
0.55	120	102	61.47	85.18	37,701	0.008
0.60	120	107	65.20	90.34	41,929	0.01
0.65	120	113	69.70	96.58	47,337	0.02
0.70	120	120	75.29	104.32	54,290	0.03
0.75	120	130	82.47	114.28	64,429	0.05
0.80	120	143	92.21	127.77	79,213	0.08
0.85	120	162	106.47	147.53	103,625	0.2
0.90	120	194	130.40	180.69	152,010	0.3

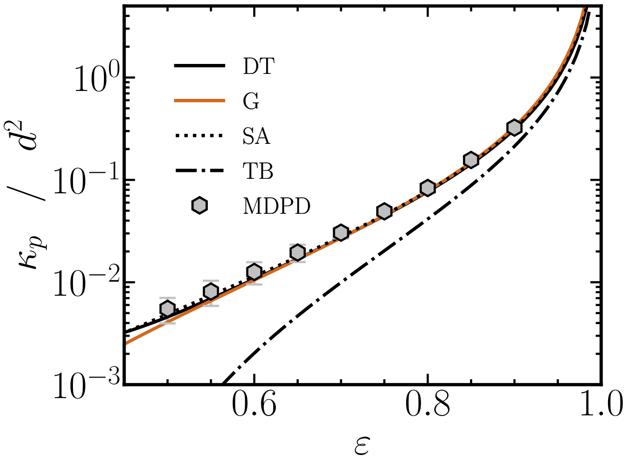

Figure S7: Permeabilities for transverse flow through hexagonal arrays of circular pillars, plotted against porosity. Results from 2D MDPD simulations (markers) are in good agreement with theories (lines) by Drummond and Tahir[1] (DT), Gebart[9](G), Sangani and Acrivos[6] (SA) and Tamayol and Bahrami[12] (TB).

S2.1.4 Irregular distributions in 2D

Table S6 lists the parameters for 2D simulations of cylindrical pillars positioned in irregular arrays. At each porosity, a set of 25 uncorrelated unit cells was generated by MC; each system contained two back-to-back copies of a unit cell. The driving force was fixed at $f_b = 0.3\epsilon/\sigma$. The dimensionless permeabilities in the last column denote averages over these sets. A plot of these permeabilities is shown in Fig. S8, along with the calculations by Chen and Papathanasiou[13] and Sangani and Yao.[14] We also observe agreement with the theory by Spielman and Goren[15] for $\varepsilon \geq 0.7$, with the lubrication theory by Koch and Ladd[16] for $\varepsilon \leq 0.55$, and with the empirical fit function by Yazdchi *et al.*[17] over the entire range. The permeabilities of the irregular arrays are remarkably similar to those of the regular lattices, which are included in Fig. 8 for comparison.

The system size dependence of the permeabilities in Table S6 was assessed by rerunning one pillar configuration per porosity as systems containing one and two consecutive copies of the same unit cell. The results, averaged over three runs per system with body forces of $f_b = 0.1$, 0.2 and $0.3\epsilon/\sigma$ are presented in Fig. S9. This plot indicates that the singular and doubled pillar arrays yield comparable permeabilities.

The parameters of the simulations of the random pillar configurations of the microfluidic chips are provided in Table S7. The permeabilities are averages over simulations with body forces of $f_b = 0.5$, 1.0, 1.5 and $2.0\epsilon/\sigma$. Comparison with the experimental data, in Fig. 6, highlights the importance of the walls.

Table S6: Simulation parameters of irregular configurations in 2D.

ε	N_{pil}	L_x [σ]	L_y [σ]	$L_{\|\|}$ [σ]	N_{part}	$\langle\kappa_p\rangle/d^2$
0.55	90	139	33.03	118.90	27,583	0.007
0.60	90	147	35.03	126.11	30,951	0.01
0.65	90	155	37.45	134.82	34,886	0.02
0.70	90	166	40.45	145.62	40,371	0.03
0.75	90	180	44.31	159.52	47,949	0.04
0.80	72	199	39.63	178.35	47,413	0.08
0.85	72	226	45.76	205.94	62,147	0.2

Table S7: Simulation parameters of the microfluidic chips in 2D.

ε	N_{pil}	L_x [σ]	L_y [σ]	$L_{\|\|}$ [σ]	N_{part}	κ_p/d^2
0.58	800	214	193.39	193.39	248,651	0.009
0.65	800	232	211.84	211.84	295,276	0.02
0.73	800	262	241.20	241.20	379,684	0.04
0.87	800	368	347.61	347.61	768,536	0.2

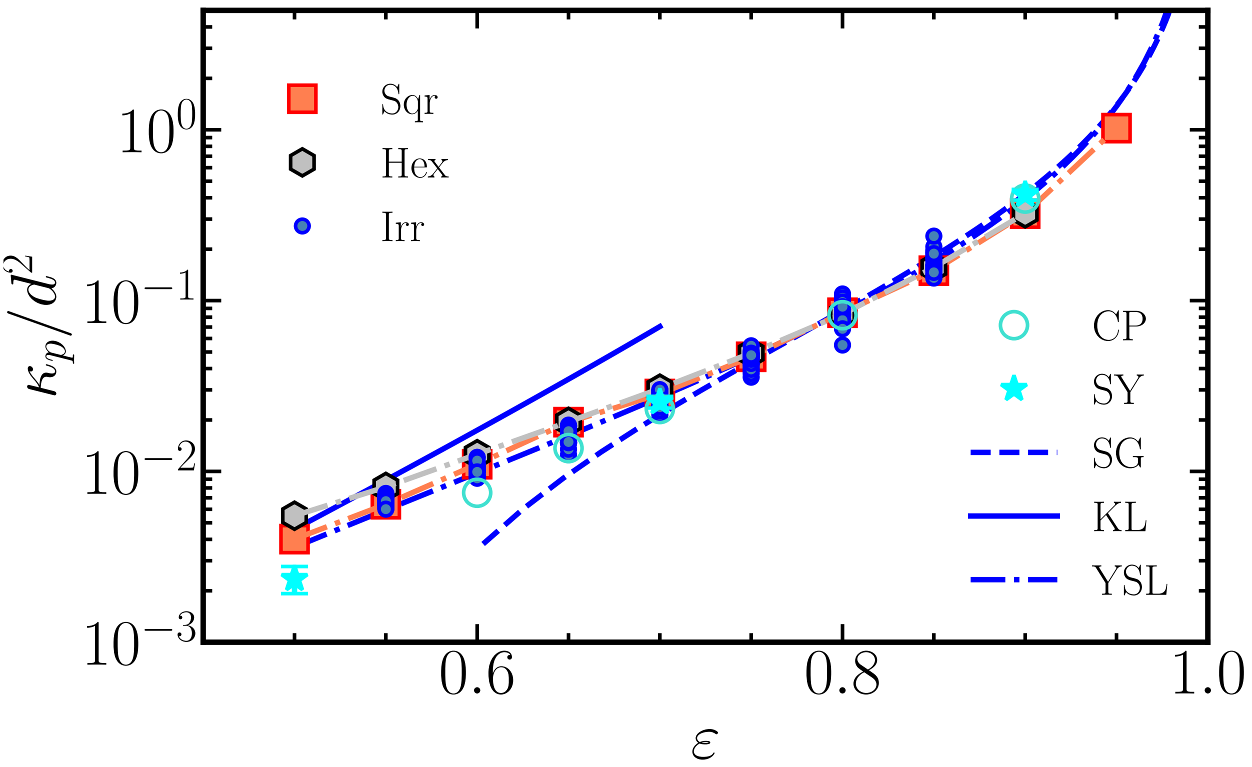

Figure S8: The permeability of irregular arrays of cylindrical pillars against porosity. Blue solid circles mark our simulation results for 25 random configurations at each porosity, the lines denote theories by Spielman and Goren[15] (SG) and Koch and Ladd[16] (KL) and a fit function by Yazdchi *et al.*[17](YSL). For comparison, we also show simulation data on irregular arrays by Chen and Papathanasiou[13] (CP) and Sangani and Yao[14] (SY), as well as our data for the square and hexagonal lattices.

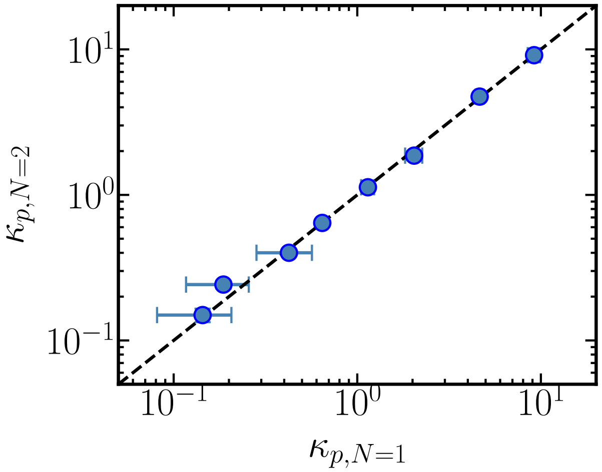

Figure S9: The comparison of κ_p calculated for irregular lattices between double ($\kappa_{p,N=2}$) and single copies ($\kappa_{p,N=1}$) of pillars.

S2.2 Simulations in 3D

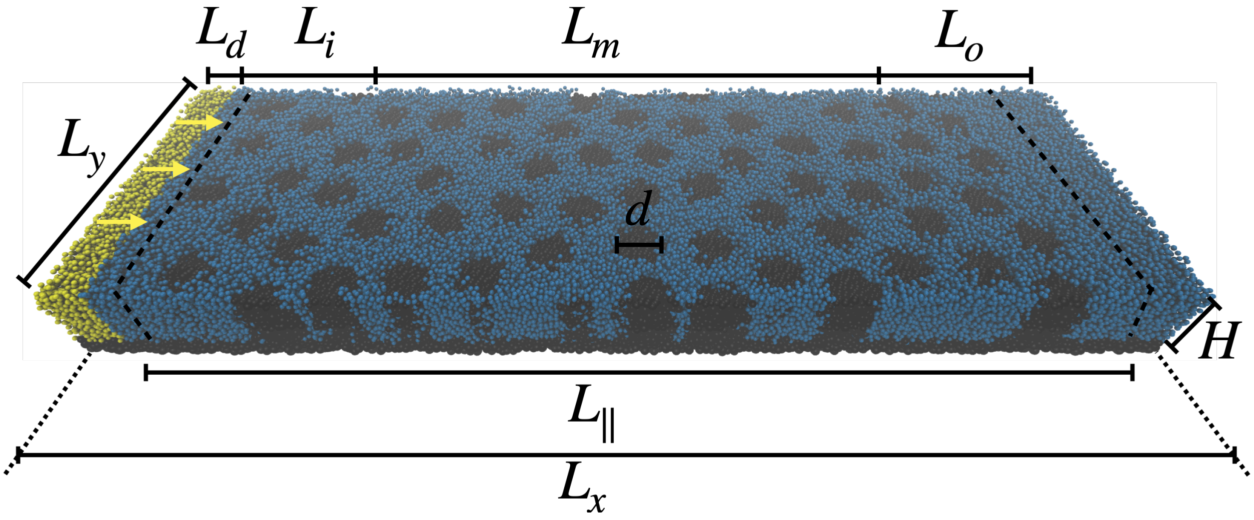

Figure S10: Snapshot of the 3D simulation set-up for fluid (blue) flowing through a disordered array of pillars (dark grey) in MDPD simulations, at a porosity of 55%. All pillars have the same diameter d and span the height H between floor (dark grey) and the ceiling (not shown) bounding the flow cell. Periodic boundary conditions apply in the x and y directions. In the driving region of length L_d (yellow), the fluid particles experience a body force f_b in the x direction (arrows). Consequently, the fluid in the remainder of the system experiences a pressure-driven flow. The length $L_{||}$ and width L_y of the pillared region match the box dimensions used in the Monte Carlo simulation generating the pillar configuration. The measurement region of length L_m is separated from the driving region by the in-flow and out-flow regions of lengths L_i and L_o, respectively.

S2.2.1 Common parameters in 3D

In the next sections we tabulate the parameters and normalized permeabilities of all 3D systems simulated in this study. Parameter common to all simulations can be found in Table S1. The various parameters listed in the ensuing tables are described in Table S8. Pillar diameters are fixed at $d = 5\sigma$, the thicknesses of the walls are $h_w = 2\sigma$.

Table S8: Parameter definitions for 3D simulations.

parameters	definition
H	height of flow channel
ε	porosity
N_{pil}	number of pillars
L_x	box length in x direction
L_y	box length in y direction
L_z	box length in z direction
$L_{\|\|}$	length of pillared region
N_{part}	total number of particles
B_{fit}/B	rescaled velocity amplitude
$\mu_{\text{eff}}^{\text{fit}}/\mu$	rescaled effective viscosity
κ_{eff}	wall-bounded permeability

S2.2.2 Square lattices in 3D

The parameters for 3D simulations of flow through pillars arranged on square lattices and square lattices rotated over 45°, bound by two walls, are tabulated in Tables S9 and S10. The calculated permeabilities in the last column of both tables denote averages over simulations with body forces of $f_b = 0.2$, 0.25 and 0.3 ϵ/σ. The last digit to B_{fit}/B, $\mu_{\text{eff}}^{\text{fit}}/\mu$ and κ_{eff}/d^2 are placed between brackets to highlight that these digits may be subject to change within the accuracy of the calculations.

Table S9: Simulation parameters of square lattices in 3D.

H [σ]	ε	N_{pil}	L_x [σ]	L_y [σ]	$L_{\|\|}$ [σ]	N_{part}	B_{fit}/B	$\mu_{\text{eff}}^{\text{fit}}/\mu$	κ_{eff}/d^2
7.5	0.55	45	80	33.03	59.45	182,929	0.87	2.9(4)	0.005
	0.60	45	84	35.03	63.06	203,723	0.77	2.1(2)	0.007
	0.65	45	88	37.45	67.41	228,100	0.75	1.7(1)	0.01
	0.70	45	93	40.45	72.81	260,310	0.87	1.9(1)	0.02
	0.75	45	100	44.31	79.76	306,464	0.90	1.9(1)	0.03
	0.80	36	110	39.63	89.17	301,641	0.91	1.8(1)	0.04
	0.85	36	123	45.76	102.97	389,581	1.2	2.5(4)	0.06
	0.90	28	119	42.04	98.08	346,142	1.3	2.3(3)	0.08
10.0	0.55	45	80	33.03	59.45	222,591	0.83(1)	2.3(3)	0.005
	0.60	45	84	35.03	63.06	247,886	0.77(1)	2.5(3)	0.007
	0.65	45	88	37.45	67.41	277,540	0.77(0)	1.9(0)	0.01
	0.70	45	93	40.45	72.81	316,777	0.88(0)	2.1(0)	0.02
	0.75	45	100	44.31	79.76	373,056	0.94(2)	2.2(1)	0.03
	0.80	36	110	39.63	89.17	367,066	0.88(1)	1.7(1)	0.05
	0.85	36	123	45.76	102.97	474,150	1.0(0)	2.1(1)	0.07
	0.90	28	119	42.04	98.08	421,252	1.1(1)	2.1(3)	0.1

Table S10: Simulation parameters of rotated square lattices in 3D.

H $[\sigma]$	ε	N_{pil}	L_x $[\sigma]$	L_y $[\sigma]$	$L_{\|\|}$ $[\sigma]$	N_{part}	B_{fit}/B	$\mu_{\mathrm{eff}}^{\mathrm{fit}}/\mu$	$\kappa_{\mathrm{eff}}/d^2$
7.5	0.55	56	81	37.37	65.39	209,454	0.85(1)	2.2(3)	0.005
	0.60	56	85	39.63	69.36	233,065	0.92(1)	2.4(2)	0.008
	0.65	56	89	42.37	74.15	260,803	0.87(1)	2.2(2)	0.01
	0.70	56	95	45.76	80.09	300,837	0.85(1)	1.8(1)	0.02
	0.75	56	102	50.13	87.73	353,688	0.96(5)	2.1(3)	0.03
	0.80	56	112	42.04	98.09	325,735	0.99(5)	2.0(3)	0.04
	0.85	42	126	48.54	113.26	423,041	1.2(2)	2.4(7)	0.06
	0.90	42	149	39.63	138.72	408,761	1.6(4)	2.9(8)	0.09
10.0	0.55	56	81	37.37	65.39	254,856	0.84(1)	2.5(3)	0.005
	0.60	56	85	39.63	69.36	283,618	0.91(2)	2.2(4)	0.008
	0.65	56	89	42.37	74.15	317,457	0.86(1)	2.1(1)	0.01
	0.70	56	95	45.76	80.09	366,165	0.87(1)	2.0(1)	0.02
	0.75	56	102	50.13	87.73	430,492	0.95(2)	2.1(3)	0.03
	0.80	36	98	42.04	98.09	346,962	0.93(2)	1.9(1)	0.05
	0.85	36	109	48.54	113.26	445,502	0.98(2)	1.7(1)	0.08
	0.90	24	129	39.63	138.72	430,515	1.2(2)	2.1(1)	0.1

S2.2.3 Irregular distributions in 3D

Table S11 lists the parameters for 3D simulations of cylindrical pillars positioned in irregular arrays, bound by two walls. At each porosity, a set of 25 uncorrelated unit cells was used; the same unit cells were also employed in the 2D simulation, with each 3D system containing a single copy only. The flow through these array were attained using a body force of $f_b = 0.3\epsilon/\sigma$.

Table S11: Simulation parameters of irregular configurations in 3D.

H [σ]	ε	N_{pil}	L_x [σ]	L_y [σ]	$L_{\|\|}$ [σ]	N_{part}	B_{fit}/B	$\mu_{\text{eff}}^{\text{fit}}/\mu$	κ_{eff}/d^2
7.5	0.55	45	80	33.03	59.45	182,929	0.89(2)	3.4(6)	0.1
	0.60	45	84	35.03	63.06	203,723	0.98(2)	3.6(4)	0.2
	0.65	45	88	37.45	67.41	228,100	0.89(1)	2.7(2)	0.3
	0.70	45	93	40.45	72.81	260,310	0.92(1)	3.2(1)	0.4
	0.75	45	100	44.31	79.76	306,464	0.89(1)	2.2(1)	0.6
	0.80	36	110	39.63	89.17	301,641	1.0(0)	2.8(1)	0.9
	0.85	36	123	45.76	102.97	389,581	0.94(3)	1.8(1)	1.5
	0.90	28	119	42.04	98.08	346,142	1.3(1)	2.5(3)	2.0
10.0	0.55	45	81	37.37	65.39	222,591	0.88(2)	3.4(5)	0.1
	0.60	45	85	39.63	69.36	247,886	0.96(1)	3.6(1)	0.2
	0.65	45	89	42.37	74.15	277,540	0.88(1)	2.5(1)	0.3
	0.70	45	95	45.76	80.09	316,777	0.90(1)	3.1(2)	0.4
	0.75	45	102	50.13	87.73	373,056	0.92(1)	2.5(1)	0.7
	0.80	36	98	42.04	98.09	367,066	0.99(1)	2.6(1)	1.1
	0.85	36	109	48.54	113.26	474,150	0.97(2)	2.0(1)	2.0
	0.90	28	129	39.63	138.72	561,325	1.1(0)	2.1(0)	2.8
12.5	0.55	45	80	33.03	59.45	262,272	0.86(0)	2.7(1)	0.1
	0.60	45	84	35.03	63.06	292,125	0.95(0)	3.2(1)	0.2
	0.65	45	88	37.45	67.41	327,051	0.89(0)	3.0(1)	0.3
	0.70	45	93	40.45	72.81	373,380	0.89(1)	3.2(1)	0.4
	0.75	45	100	44.31	79.76	439,680	0.92(0)	2.5(1)	0.8
	0.80	36	110	39.63	89.17	432,608	0.99(1)	2.8(0)	1.2
	0.85	36	123	45.76	102.97	558,808	0.95(2)	2.0(1)	2.4
	0.90	28	119	42.04	98.08	661,617	1.02(1)	2.0(0)	3.6

The flow resistance due to the pillars can be calculated by 3D simulations without walls, using periodic boundary conditions along the z direction instead. In view of the translation symmetry along the z direction, it is more efficient to use 2D simulations. To assess the agreement between the 2D and 3D simulations, one random unit cell per porosity was simulated in both 2D and 3D. The parameters of these simulations are listed in Table S12. The permeabilities represent averages over three independent runs with body forces $f_b = 0.02$, 0.03 and $0.05\epsilon/\sigma$ in 2D and $f_b = 0.1$, 0.2 and $0.3\epsilon/\sigma$ in 3D. Figure S11 shows the close adherence between the permeabilities obtained in 2D and 3D. Note that the two sets of simulations use two distinct fluids, differing *e.g.* in their viscosity, and different particle-based representations of the same pillar configurations.

Table S12: Simulation parameters of irregular configurations without walls in 2D and 3D.

ε	N_{pil}	L_x $[\sigma]$	L_y $[\sigma]$	L_z^{3D} $[\sigma]$	$L_{\|\|}$ $[\sigma]$	$N_{\mathrm{part}}^{\mathrm{2D}}$	$N_{\mathrm{part}}^{\mathrm{3D}}$	$\kappa_p^{\mathrm{2D}}/d^2$	$\kappa_p^{\mathrm{3D}}/d^2$
0.55	45	80	33.03	5	59.45	15,883	79,412	0.2	0.1
0.60	45	84	35.03	5	63.06	17,695	88,434	0.24	0.20
0.65	45	88	37.45	5	67.41	19,818	98,999	0.4	0.5
0.70	45	93	40.45	5	72.81	22,621	112,993	0.7	0.6
0.75	45	100	44.31	5	79.76	26,650	133,060	1.1	1.1
0.80	36	110	39.63	5	89.17	26,219	130,963	1.9	1.9
0.85	36	123	45.76	5	102.97	33,851	169,124	4.7	4.4

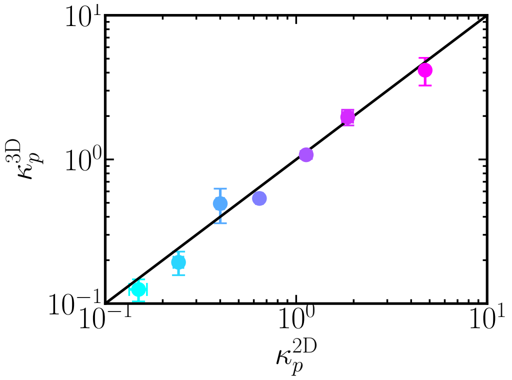

Figure S11: Permeabilities of disordered pillar arrays κ_p, in the absence of walls, for 2D and 3D simulation with identical pillar arrangements. Horizontal (invisible) and vertical error bars correspond to standard deviations. Along the solid line, representing the ideal agreement between 2D and 3D simulations, the porosity increases from $\varepsilon = 0.55$ in the bottom-left to 0.85 in the top-right.

S3 Theories

S3.1 Permeabilities of lattices in 2D

Table S13 and S14 list theoretical expressions for the rescaled permeability κ_p/d^2 through cylinders placed on lattices. Some theories are conveniently expressed in porosity, others in the solid volume fraction $\phi = 1 - \varepsilon$.

Table S13: Theoretical permeabilities of square lattices in 2D.

Author(s)	Abbrev.	κ_p/d^2
Drummond and Tahir[1]	DT	$\frac{1}{32\phi}\left(-\ln\phi - 1.476 + \frac{2\phi - 0.796\phi^2}{1 + 0.489\phi - 1.605\phi^2}\right)$
Bruschke and Advani[3]	BA-1	$\frac{1}{32\phi}\left(-\ln\phi - 1.500 + 2\phi - \frac{\phi^2}{2}\right)$
Kuwabara[4]	K	$\frac{1}{32\phi}\left(-\ln\phi - 1.500 + 2\phi - \frac{\phi^2}{2}\right)$
Hasimoto[5]	H	$\frac{1}{32\phi}\left(-\ln\phi - 1.476 + 2\phi + O(\phi^2)\right)$
Sangani and Acrivos[6]	SA	$\frac{1}{32\phi}\left(-\ln\phi - 1.476 + 2\phi - 1.774\phi^2 + 4.076\phi^3 + O(\phi^4)\right)$ (small ϕ) $\frac{1}{9\sqrt{2}\phi}\left(1 - \sqrt{\frac{\phi}{\phi_{\max}}}\right)^{5/2}$ (large ϕ)
Tsay and Weinbaum[7]	SATW	$0.0143\,\Delta^{2.377}$, with $\Delta = \sqrt{\frac{\pi}{\phi}} - 2$ (interpolation formula to SA)
Happel[18]	HP	$\frac{1}{32\phi}\left(-\ln\phi - \frac{1-\phi^2}{1+\phi^2}\right)$
Gebart[9]	G	$\frac{4}{9\pi\sqrt{2}}\left(\sqrt{\frac{1-\varepsilon_{\min}}{1-\varepsilon}} - 1\right)^{5/2}$, with $\varepsilon_{\min} = 1 - \frac{\pi}{4}$
Bruschke and Advani[3]	BA-2	$\frac{\left(1-l^2\right)^2}{12l^3}\left(3l\frac{\tan^{-1}\lambda}{\sqrt{1-l^2}} + \frac{l^2}{2} + 1\right)^{-1}$, $l^2 = \frac{4}{\pi}(1-\varepsilon)$, $\lambda = \sqrt{\frac{1+l}{1-l}}$
Lee and Yang[10]	LY	$\frac{\varepsilon^3(\varepsilon - 0.2146)}{31(1-\varepsilon^{1.3})}$
Sahraoui and Kaviany[11]	SK	$\frac{0.0152\pi\varepsilon^{5.1}}{1-\varepsilon}$
Tamayol and Bahrami[12]	TB	$\frac{0.16}{\sqrt{1-\phi}}\left(\frac{\pi}{4\phi} - 3\sqrt{\frac{\pi}{4\phi}} + 3 - \sqrt{\frac{4\phi}{\pi}}\right)$

Table S14: Theoretical permeabilities of hexagonal lattices in 2D.

Author(s)	Abbrev.	κ_p/d^2
Drummond and Tahir[1]	DT	$\frac{1}{32\phi}\left(-\ln\phi - 1.497 + 2\phi - \frac{\phi^2}{2} - 0.739\phi^4 + \frac{2.534\phi^5}{1+1.2758\phi}\right)$
Sangani and Acrivos[6]	SA	$\frac{1}{32\phi}\left(-\ln\phi - 1.490 + 2\phi - \frac{\phi^2}{2} + O(\phi^3)\right)$
Gebart[9]	G	$\frac{4}{9\pi\sqrt{6}}\left(\sqrt{\frac{1-\varepsilon_{\min}}{1-\varepsilon}} - 1\right)^{5/2}$, with $\varepsilon_{\min} = 1 - \frac{\pi}{2\sqrt{3}}$
Tamayol and Bahrami[12]	TB	$\frac{0.16}{\sqrt{1-\phi}}\left(\frac{\pi}{3\sqrt{3}\phi} - 3\sqrt{\frac{\pi}{3\sqrt{3}\phi}} + 3 - \sqrt{\frac{3\sqrt{3}\phi}{\pi}}\right)$

S3.2 Permeabilities of irregular distributions in 2D

Table S15 lists theoretical expressions for the rescaled permeability κ_p/d^2 of irregular arrays. The YSL expression in the bottom row is explored below.

Table S15: Theoretical permeabilities of irregular distributions in 2D.

Author(s)	Abbrev.	κ_p/d^2
Spielman and Goren[15]	SG	$\frac{1}{8x} + \frac{1}{2\sqrt{x}}\frac{K_1(1/2\sqrt{x})}{K_0(1/2\sqrt{x})} = \frac{1}{16\phi x}$ In this implicit equation for $x = \kappa_p/d^2$, $K_n(x)$ denotes the n^{th} order Bessel function of the second kind.
Koch and Ladd[16]	KL	$\frac{\sqrt{2}}{17}\frac{\varepsilon_c^{5/2}}{\phi}$, for $\varepsilon < 0.6$. We refer to Ref. 16 for $\varepsilon_c(\phi)$. $\frac{2.76}{\phi\exp(11.1\phi)}$ (fit to their Fig. 21).
Yazdchi *et al.*[17]	YSL	$0.2\chi(\gamma_2)\gamma_2^{5/2}$, with $\gamma_2 = 0.26\phi^{0.6790} - 0.47$ and $\chi(\gamma_2) = 1 - 0.5e^{-3.0\gamma_2}$.

The theory by Gebart[9] (G) for regular lattices takes the form $\kappa_p/d^2 = C\gamma^{5/2}(\varepsilon)$, with

$$\gamma = \sqrt{\frac{1-\varepsilon_{\text{min}}}{1-\varepsilon}} - 1, \tag{S1}$$

and where the proportionality factor C and minimum porosity ε_{min} vary with the lattice structure, see Tables S13 and S14. The above square-root describes the scaling of the lattice spacing with porosity, hence the distance between n^{th}-nearest neighbour pillars is given by $D_n(\varepsilon) = D_n(\varepsilon_{\text{min}})(\gamma + 1)$. Yazdchi *et al.*[17] use the latter relation to extract the 'scaling' of irregular pillar arrangements from the mean distance $\langle D_n \rangle$ between n^{th}-nearest neighbour pillars,

$$\gamma_n = \frac{\langle D_n \rangle}{d} - 1. \tag{S2}$$

A good agreement with the permeability was recovered when using the next-nearest neighbour, $n = 2$, whose mean distance was well fitted by

$$\langle D_2 \rangle = \bar{D}_2 \left[1 + \phi_2 \left(\frac{1-\varepsilon}{1-\varepsilon_{\text{min}}^{\text{irr}}} \right)^{\xi_2} \right] d, \tag{S3}$$

with $\bar{D}_2 = 0.5303$, $\phi_2 = 0.3372$, $\xi_2 = 0.6790$ and $\varepsilon_{\text{min}}^{\text{irr}} = 0.4167$. This function provides a good description of the next-nearest pillar distances in our irregular arrays, as illustrated in Fig. S12(a). The plot also shows that the standard deviation in the next-nearest neighbour distance increases with porosity, as expected. Inserting of this γ_2 as γ in Gebart's theory yields a good description of the permeability of irregular arrays for $C = 0.2$, see Fig. S12(b). The agreement improves upon multiplication with a fit function $\chi(\gamma_2)$,[17] see Fig. S12(b) and Table S15 (YSL).

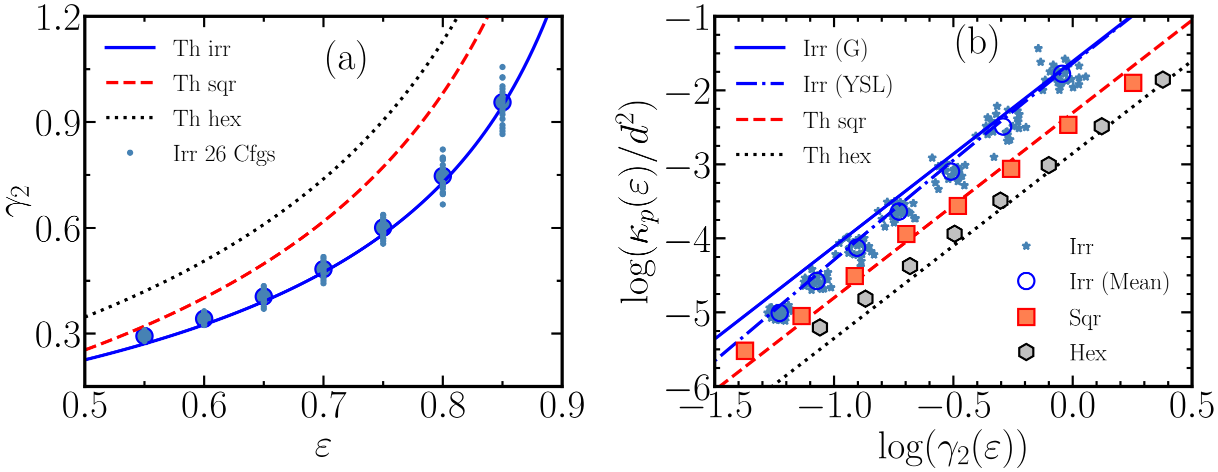

Figure S12: (a) The mean next-nearest neighbour distance $\langle D_2 \rangle$, plotted here as $\gamma_2 = \langle D_2 \rangle/d - 1$, as a function of porosity ε for three arrangements of cylindrical pillars. The theoretical (Th) expressions for square (red dashed, sqr) and hexagonal lattices (black dotted, hex) match exactly with the simulation results (not shown). For irregular lattices, small blue solid dots mark averages for 25 random configurations per porosity, with the larger blue circles denoting the average over these configurations at each porosity. The solid line represents Eq. S3. (b) The dimensionalized permeability as a function of γ_2. The red dashed and black dotted lines represent Gebart's (G) theories for square and hexagonal lattices, respectively. The blue solid line shows the extension of Gebart's to irregular lattices by Yazdchi *et al.*, based on the mean next-nearest neighbour distance, while the blue dash-dotted line illustrates their full fit expression (YSL). The simulation data for the irregular pillar arrangements are shown as 25 blue solid dots at every porosity, which appear in the plot as clusters.

S3.3 Permeabilities of lattices in 3D

Lee and Fung[19] solved the Stokesian flow around a single cylinder between two walls as an infinite series, valid when the distance between the walls H is less than ∼10 times the pillar radius R. The two leading terms of this series provide a good approximation when $R < H$. Lee[20] used this solution to describe the flow resistance by a rotated square lattice of cylinders between walls, see Fig. S13, in the limit of the interpillar spacing far exceeding the diameter of the pillars. Tsay and Weinbaum[7] used the theory by Lee and Fung to derive a general solution for the flow resistance by a rotated square lattice between flat walls, in terms of an infinite series. Their result converged to the expression by Lee and Sangani & Acrivos in the limits of high and low porosity, respectively, suggesting that a more compact expression could be obtained by interpolating between these limits. This they realized by an extrapolation of Lee's expression (LTW in Table S16) and a fit to the expression by Sangani and Acrivos (SATW), to arrive at the interpolation formula (TW). In the table, the drag expressions by these authors have been inverted to obtain permeabilities. These expressions compare very well against the simulation results, see Fig. S14, reaching their maximum relative deviation in the interpolation region between the two limiting regimes.

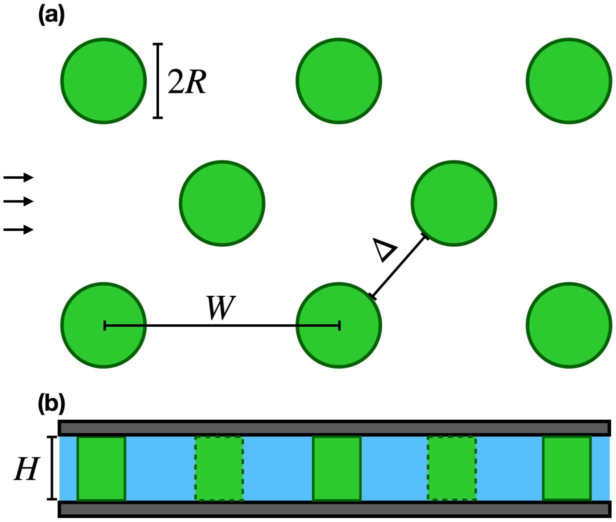

Figure S13: Schematics of the rotated square lattice between flat walls, showing cut-sections of (a) the top-view and (b) the side-view of flow channel. The arrows indicate the direction of flow.

Table S16: Theoretical permeabilities of a rotated square lattice between walls

Abbrev.	$\kappa_{\mathrm{eff}}/\kappa_w$
SATW (pillar dominated)	$\frac{1}{f_{2d}}$ where $f_{2d} = \frac{H^2}{6W^2} f'_{2d}$ with $f'_{2d} = \frac{F_d}{\mu u_s} \approx \frac{54.95}{\phi \Delta^{2.377}}$ an approximation to SA.[6]
LTW (wall dominated)	$\frac{1}{f_{3d}}$ where the expression $f_{3d} = \frac{1 - b_1\phi}{1 + b_1\phi}$ by Lee[20] for $\phi < \phi_\Delta$ is extrapolated as $f_{3d} = \frac{1 - b_1\phi}{1 + b_1\phi} - 2b_1 \frac{\phi - \phi_\Delta}{(1 + b_1\phi_\Delta)^2}$ for $\phi > \phi_\Delta$, with $b_1 = -\frac{K_2(\pi R/H)}{K_0(\pi R/H)}$ and $\phi_\Delta = \phi(\Delta = H)$. $K_n(x)$ denotes the n^{th} order Bessel function of the 2^{nd} kind
TW (interpolation)	$\frac{1}{(f_{2d}^n + f_{3d}^n)^{1/n}}$ where $n = \frac{B}{0.1918 + 0.3308B}$ with $B = \frac{H}{2R}$.

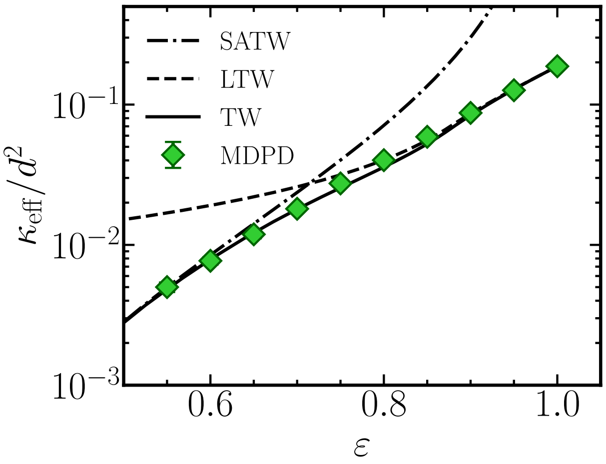

Figure S14: Effective permeabilities of the flow through a rotated square lattice confined between top and bottom walls. The effective permeabilties are normalized by the square of the pillar diameters.

S4 Comparison with experiments

S4.1 Comparison with our experiments

Figure S15 shows comparisons between experimental and calculated effective permeabilities, supplementing the numerical results in Fig. 13.

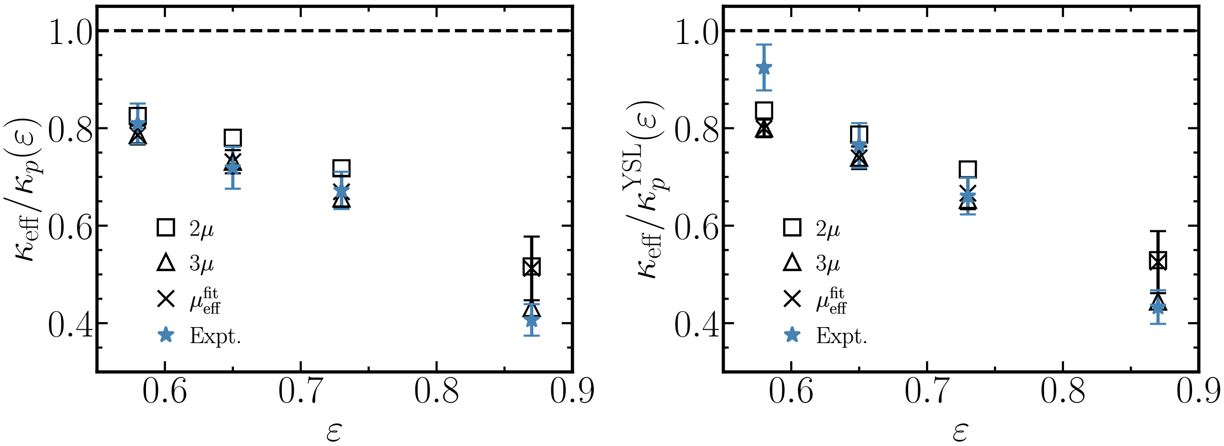

Figure S15: Comparison of the experimental permeability κ_{eff} in this work with numerical results and expressions for the effective permeability. (Left) Applicatons of Brinkman's theory combining the simulated 2D pillar permeability $\kappa_p(\varepsilon)$ with the theoretical amplitude B and various values of the effective viscosity. (Right) Applicatons of Brinkman's theory combining the pillar permeability of Yazdchi *et al.*[17] (YSL in Table S15) with the theoretical amplitude B and various values of the effective viscosity.

S4.2 Comparison with experiments by Gunda *et al.*

Gunda *et al.*[21] etched square lattices of cylindrical pillars in silicon. Their systems provide a convenient testing ground for the application of Brinkman's theory, supplementing the irregular arrays studied in the main text. The experimental data by Gunda *et al.* are collected in Table S17. The plot in Fig. S16(a) shows that the effective permeability follows the systematic rise of the theoretical prediction for a square lattice by Tamayol and Bahrami,[12] though the latter systematically exceeds the experimental data. Combining this prediction with Brinkman's correction for the walls, using the constant effective viscosity $\mu_{\mathrm{eff}} = 2.1\mu$ suggested by Fig. 11, yields effective permeabilities in better agreement with the experimental data. We note that whereas the Brinkman correction predicts a decreasing ratio $\kappa_{\mathrm{eff}}/\kappa_{\mathrm{sq}}^{\mathrm{TB}}$ with increasing porosity, the experimental data suggest a more constant ratio, see Fig. S16(b). It is conceivable that the limited width of the channel, with nine pillars per row, contributes to the deviations from theory, especially at the higher porosities.[22]

A second comparison with data from the literature, *i.e.* simulations by Wagner *et al.*,[22] is presented in the main text, see Fig. 14.

Table S17: Experimental parameters for square lattices between walls by Gunda *et al.*

ε	d [μm]	H [μm]	κ_{eff} [10^{-10} m^2]
0.50	100	98.4	0.2
0.70	50	98.4	0.4
0.80	50	98.4	1.5
0.90	30	98.4	1.7
0.95	30	98.4	7.0

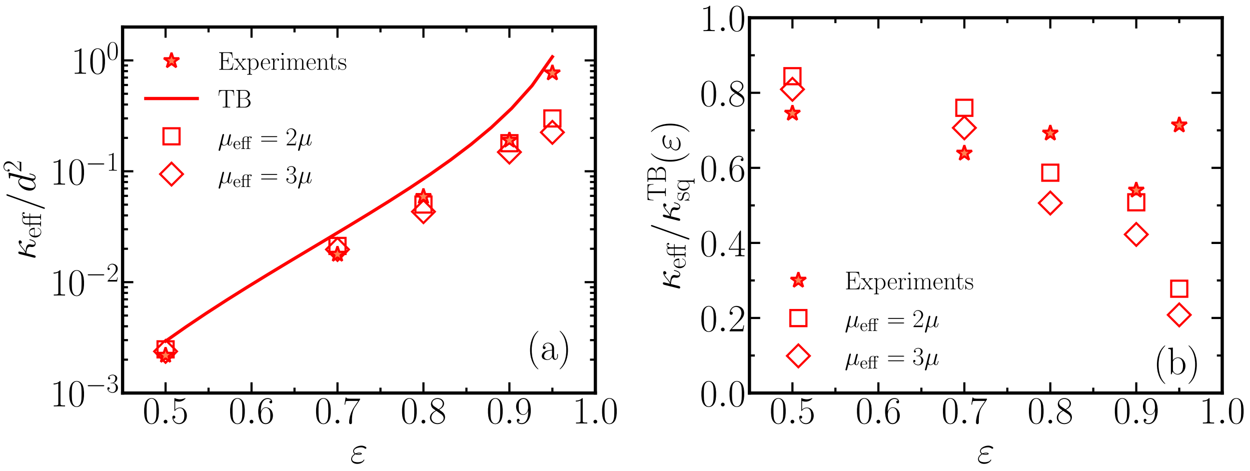

Figure S16: (a) Comparison of the effective permeability of square arrays measured by Gunda *et al.* with the permeability of square pillar arrays following the theory by Tamayol and Bahrami (TB, see Table S13) and the combination of said theory with Brinkman's theory. (b) The experimental and calculated effective permeability normalized by the theoretical permeability of the square pillar array (TB), to highlight the impact of the walls for two effective viscosities.

Bibliography

[1] J. E. Drummond and M. I. Tahir, *Int. J. Multiphase Flow*, 1984, **10**, 515–540.

[2] K. Yazdchi, S. Srivastava and S. Luding, *Int. J. Multiphase Flow*, 2011, **37**, 956–966.

[3] M. V. Bruschke and S. G. Advani, *J. Rheol.*, 1993, **37**, 479–498.

[4] S. Kuwabara, *J. Phys. Soc. Japan*, 1959, **14**, 527–532.

[5] H. Hasimoto, *J. Fluid Mech.*, 1959, **5**, 317–328.

[6] A. S. Sangani and A. Acrivos, *Int. J. Multiphase Flow*, 1982, **8**, 193–206.

[7] R.-Y. Tsay and S. Weinbaum, *J. Fluid Mech.*, 1991, **226**, 125–148.

[8] J. Happel, *AIChE J.*, 1959, **5**, 174–177.

[9] B. R. Gebart, *J. Compos. Mater.*, 1992, **26**, 1100–1133.

[10] S. Lee and J. Yang, *Int. J. Heat Mass Transfer*, 1997, **40**, 3149–3155.

[11] M. Sahraoui and M. Kaviany, *Int. J. Heat Mass Transfer*, 1994, **35**, 927–943.

[12] A. Tamayol and M. Bahrami, *Phys. Rev. E*, 2011, **83**, 046314.

[13] X. Chen and T. D. Papathanasiou, *Transport in Porous Media*, 2008, **71**, 233–251.

[14] A. S. Sangani and C. Yao, *The Physics of Fluids*, 1988, **31**, 2435–2444.

[15] L. Spielman and S. L. Goren, *Environmental Science & Technology*, 1968, **2**, 279–287.

[16] D. L. Koch and A. J. C. Ladd, *Journal of Fluid Mechanics*, 1997, **349**, 31–66.

[17] K. Yazdchi, S. Srivastava and S. Luding, *Composites A*, 2012, **43**, 2007–2020.

[18] J. Happel and N. Epstein, *Ind. Eng. Chem. Res.*, 1954, **46**, 1187–1194.

[19] J. S. Lee and Y. C. Fung, *J. Fluid Mech.*, 1969, **37**, 657–670.

[20] J. S. Lee, *J. Biomech.*, 1969, **2**, 187–198.

[21] N. S. K. Gunda, J. Joseph, A. Tamayol, M. Akbari and S. K. Mitra, *Microfluid. nanofluidics*, 2013, **14**, 711–721.

[22] A. Wagner, E. Eggenweiler, F. Weinhardt, Z. Trivedi, D. Krach, C. Lohrmann, K. Jain, N. Karadimitriou, C. Bringedal, P. Voland *et al.*, *Transp. Porous Media*, 2021, 1–23.